Damage and recovery of calcite rocks deformed in the cataclastic regime

A. SCHUBNEL[1,2], J. FORTIN[2], L. BURLINI[3] & Y. GUÉGUEN[2]

[1]*Lassonde Institute, University of Toronto, 170 College Street, Toronto, Ontario, Canada, M5S 3E3 (e-mail: alexandre.schubnel@utoronto.ca)*
[2]*Laboratoire de Géologie, Ecole Normale Supérieure, 24 rue Lhomond, 75005 Paris, France*
[3]*Experimental Rock Deformation Laboratory, ETH, Sonneggstrasse 5, 8092 Zürich, Switzerland*

Abstract: Compressional and shear wave velocities have been measured during the experimental deformation of Carrara marble and Solnhofen limestone in the cataclastic regime, both in dry and wet conditions at room temperature. Measurements were performed under hydrostatic conditions (up to 260 MPa confining pressure and 10 MPa pore pressure) during triaxial loading (at the constant strain rate of 10^{-5} s^{-1}) as well as during differential stress relaxation. During a full cycle, our results show that the seismic velocities first increase as effective mean stress increases. However, when the stress onset of cataclastic deformation was reached, elastic velocities showed rapid decrease due to stress-induced damage in the rock. During stress relaxation tests we observed an increase of elastic velocities with time, which suggested a fast 'recovery' of the microstructure. A substantial and rapid drop in the velocities occurred when reloading, suggesting that the previous 'recovery' was only transient. Subsequent relaxation tests showed other marked increases in velocities. These experimental results suggest that during the deformation of low-porosity calcite-rich rocks, dilatant (crack opening and frictional sliding) and compaction micro-mechanism (pore closure) compete. Evolutions of elastic properties (mainly sensitive to crack density) and macroscopic volumetric strain (more sensitive to porosity) are therefore not systematically correlated and depend on the strain rate, the solid stress conditions and the pore pressure.

Interest in the brittle–ductile transition has increased considerably in recent years, in large part due to the fact that the maximum depth of seismicity corresponds to a transition in the crust and in the upper mantle from seismogenic brittle failure to aseismic cataclastic flow, i.e. from localized to homogeneous deformation. The mechanics of the transition depends both on some extrinsic variable (state of solid stress, pore pressure, temperature, fluid chemistry and strain rate) and intrinsic parameters (crack and dislocation density, modal composition of the rock or porosity, for example). The deformation mechanisms operative during the transition occur on scales ranging from microscopic to macroscopic, and have a profound influence on the spatio-temporal evolution of stress and deformation during the earthquake cycle, as well as in the coupling of crustal deformation and fluid transport.

Limestones and marbles, even the ones with very low porosity like Carrara marble, have been studied widely in the past as they can undergo a brittle–plastic transition at room temperature for confining pressures easily attainable in the laboratory (Robertson 1955; Paterson 1958; Heard 1960; Rutter 1974). Such a behaviour is probably due to the fact that calcite requires relatively low shear stresses to initiate twinning and dislocation glide, even at room temperature (Turner *et al.* 1954; Griggs *et al.* 1960). In consequence, many previous studies have already documented the mechanical behaviour of both Carrara marble (Fredrich *et al.* 1989, 1990) and Solnhofen limestone (Robertson 1955; Heard 1960; Byerlee 1968; Edmond & Paterson 1972; Rutter 1972; Fisher & Paterson 1992; Renner & Rummel 1996; Baud *et al.* 2000). These studies have demonstrated that porosity change and failure mode are intimately

related. In the cataclastic flow regime, Baud *et al.* (2000) showed that the pore space may either dilate or compact in response to an applied stress.

In the present study, compressional and shear wave velocities have been measured during both hydrostatic and triaxial experiments performed on Carrara marble and Solnhofen limestone at room temperature. Our new set of data show that during cataclastic deformation, elastic wave velocities show large variations. Damage (a decrease in the effective elastic properties) and apparent recovery of those properties are transient phenomena that depend mainly on the the stress history, the pore pressure and the strain rate. Elastic properties, macroscopic strain and post-deformation microstructural analysis were put together and may have implications for the understanding of fault gouge behaviour and, thus, direct consequences on the

understanding of fault zones and the earthquake cycle.

Experimental set-up

Here we describe for the first time the triaxial cell installed at the Laboratoire de Géologie of Ecole Normale Supérieure (ENS) (Paris, France). This is a prototype that was designed and constructed by the company Geodesign, based in Roubaix, France.

Description of the vessel

The Geodesign triaxial cell can reach a confining pressure of 300 MPa (Fig. 1) and the confining medium is oil. The confining pressure is servo-controlled with an accuracy of 0.1 MPa. Axial load is achieved through an auto-compensated
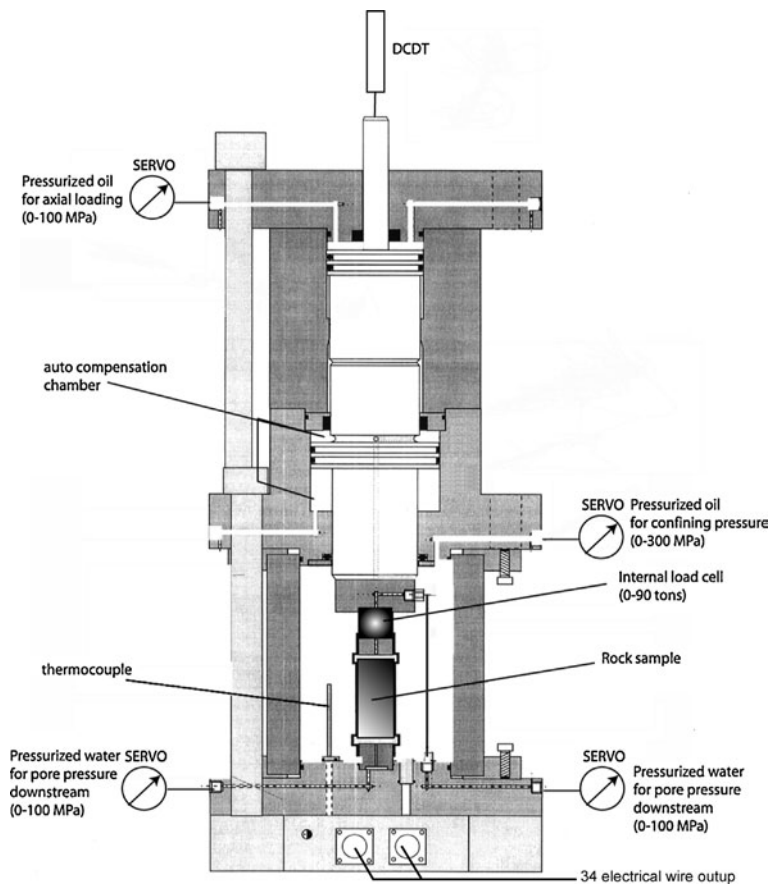

Fig. 1. Schematic diagram of the triaxial high-pressure cell installed at the Laboratoire de Géologie of Ecole Normale Supérieure of Paris (France).

(i.e. that does not move when confining pressure varies) hydraulic piston that can be servo-controlled in either strain or stress. Maximum load is 90 tons, which corresponds to 717 MPa for a 40 mm-diameter sample. An internal load cell, manufactured by AMC automation, enables measurement of the applied load directly on top of the sample with an accuracy of approximately 1 MPa. Minimum strain rate is 10^{-6} s^{-1} and is monitored externally through two LVDTs (Linear Variable Differential Transformers) placed on top of the piston, outside the vessel. Minimum axial loading rate is 0.01 MPa s^{-1} and is servo-controlled using two pressure transducers.

Both confining and axial pressure systems are driven by the same hydraulic ram (0–35 MPa) along with two intensifiers: 35–300 MPa for the confining pressure, 35–100 MPa for the axial pressure. Pore pressure is driven by two precision volumetric pumps manufactured by Maxitechnologies. Pore fluid is introduced into the sample through hardened steel end pieces placed on the top and bottom of the rock sample. Maximum pore pressure in the system is 100 MPa. Both pumps can be controlled either in pressure (0.01 MPa precision), in flow (minimum flow is 0.1 h^{-1}) or in volume (precision is approximately 0.005 cm^3).

The main advantage of the ENS triaxial apparatus is its 34 electric feedthroughs that can allow simultaneous measurements of seismic velocities in several directions, as well as other properties across the sample (for example local strains). Finally, a thermocouple enables the temperature in the oil chamber to be monitored.

Sample set-up and preparation

Four samples (two of Carrara marble and two of Solnhofen limestone) were cored perpendicular to the bedding. All samples measured 80 mm in length and 40 mm in diameter. The end surfaces were rectified and polished to ensure homogeneous loading and minimum friction during testing. The porosity of each sample was measured using a double saturation technique. Four parallel flat surfaces were machined along the cylinder of the sample at 90° to one another. Compressional and shear wave velocities were measured in each direction under dry atmospheric pressure conditions. Average initial porosity and velocity values of Carrara marble and Solnhofen limestone used in this study are summarized in Table 1.

During an experiment, axial and radial strains were measured directly on the sample's surface using strain gauge pairs (TML FLA-20, Tokyosokki). Each of which was mounted in a 1/4 Wheatstone bridge; strain measurement accuracy was approximately 10^{-6}. Volumetric strain was calculated using strain gauges according to the formula $\varepsilon_v = \varepsilon_a + 2 \times \varepsilon_r$, where ε_a is the axial strain measurement from longitudinal strain gauge, ε_r is the radial strain measurement from horizontal strain gage and ε_v the calculated volumetric strain.

P, SV and SH elastic wave velocities were measured perpendicular to compression axis, along diameters of the sample, using couples of source–receiver lead-zirconate piezoceramic transducers (PZTs) (Fig. 2). PZTs (PI255, PI ceramics, 1 MHz eigenfrequency) were glued directly onto the flat surfaces of each sample and positioned with approximately 0.5 mm accuracy, whilst the distance between opposite (paired) PZTs from which the velocities were calculated was measured within 0.01 mm. Compressional PZTs were 5 mm diameter discs, 1 mm thick; Shear PZTs were plates (5 × 5 × 1 mm). Pulse was generated by a Sofranel source generator (up to 370 V at 1 MHz frequency).

For each velocity measurement, more than 200 waveforms were stacked on a digital oscilloscope, in order to increase the signal/noise

Table 1. *Composition, initial porosity, grain size and elastic wave velocities at atmospheric pressure under dry conditions of Carrara marble and Solnhofen limestone used in this study*

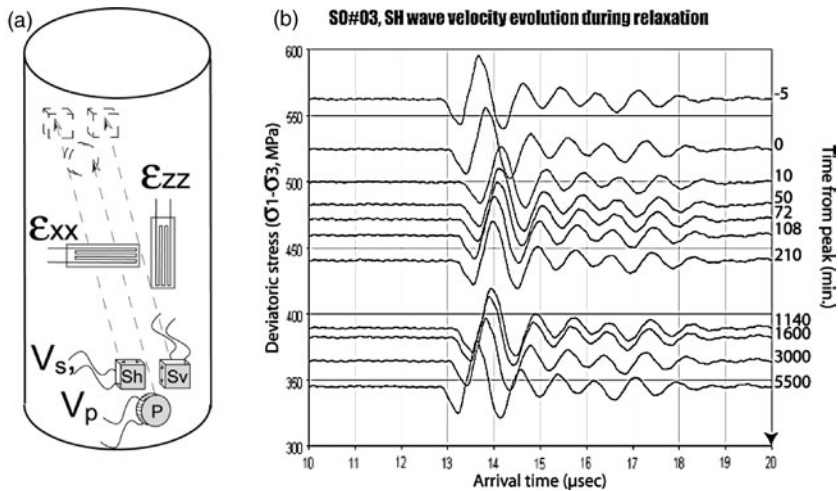|	Carrara marble	Solnhofen limestone
Composition	>99% calcite	>99% calcite
Initial porosity (%)	0.5	4.5
Grain size (μm)	*c.* 150	*c.* 5
Mean initial, V_p (km s^{-1})	5.92	5.64
Mean initial, V_s (km s^{-1})	3.23	3.05
Incompressibility, K (dynamic, GPa)	57.5	50.4
Poisson ration, ν (dynamic)	0.29	0.29
Initial P wave anisotropy (%)	<1	*c.* 2

Fig. 2. (**a**) Schematic view of prepared sample with attached strain gauges and PZT sensors. Elastic wave velocities were measured along diameters. All samples measured 80 mm in length, 40 mm in diameter. An example of obtained waveforms for SH waves is shown in (**b**).

ratio. In such conditions, the absolute velocity error bar was of the order of a few per cent, but relative error in between two consecutive measurements was lowered to 0.5% using a double-picking technique. An example of obtained waveform recordings is shown in Figure 2b. Inside the vessel, the sample was covered with a Neoprene jacket that insulated it from the confining oil.

Experimental procedure

Two experiments (So#02 and Ca#01) were carried out under dry conditions at a confining pressure of to 200 MPa on Solnhofen limestone and Carrara marble, respectively. Two additional experiments (So#03 and Ca#02) were carried out in the saturated regime in which rock samples were first subjected to 15 MPa confining pressure and 10 MPa pore pressure for a minimum of 2 days in order to attain full saturation. Confining pressure was then raised up to 260 MPa, and the sample was left overnight for pore pressure equilibration before the triaxial loading cycle.

All triaxial cycles performed in this study were strain-rate controlled at a constant strain rate of 10^{-5} s^{-1}. During each experiment several relaxation tests were also performed in order to investigate possible recovery of the sample. During the stress relaxation tests, the piston position was locked and the differential stress decreased due to deformation of the sample. These relaxation tests lasted from 1 h to several days in the case of saturated samples Ca#02 and So#03.

Experimental results

Figure 3 illustrates stress–strain curves for the four tests. Plastic deformation was reached for smaller differential stress in Carrara marble than in Solnhofen limestone. Hardening
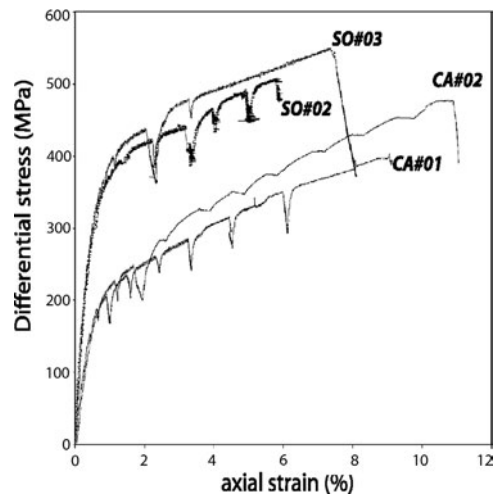

Fig. 3. Differential stress v. axial strain in the four tests presented in this paper. Ca#01 and Ca#02 were experiments performed on Carrara marble in dry ($P_c = 200$ MPa) and wet ($P_c = 260$ MPa, $P_p = 10$ MPa) conditions, respectively. So#02 (dry, $P_c = = 200$ MPa) and So#03 (wet, $P_c = 260$ MPa, $P_p = 10$ MPa) were experiments performed on Solnhofen limestone.

coefficient increases with confining pressure and figure shows that several relaxation tests were performed during the testing of each sample.

During the four experiments, strains, stresses and elastic wave velocities were continuously measured. This section presents a non-exhaustive compilation of our results in terms of coupled evolution of elastic wave velocities and volumetric strain v. effective mean stress, differential stress and time (Elastic wave velocities were measured perpendicular to the main compressive axis, and S wave velocities refer to the average between S_h and S_v wave measurements).

Volumetric strain and elastic wave velocities v. effective mean stress

We will refer to onset of dilatancy C' and onset of compaction C^* (as defined by Wong *et al.* 1997) as the stress onset (in differential stress for a given effective mean stress) at which macroscopic inelastic dilatancy and compaction were first observed. The onset of cataclastic dilatancy $C^{*'}$ is defined as the stress value at which cataclastic deformation turned from macroscopically compactive to dilatant.

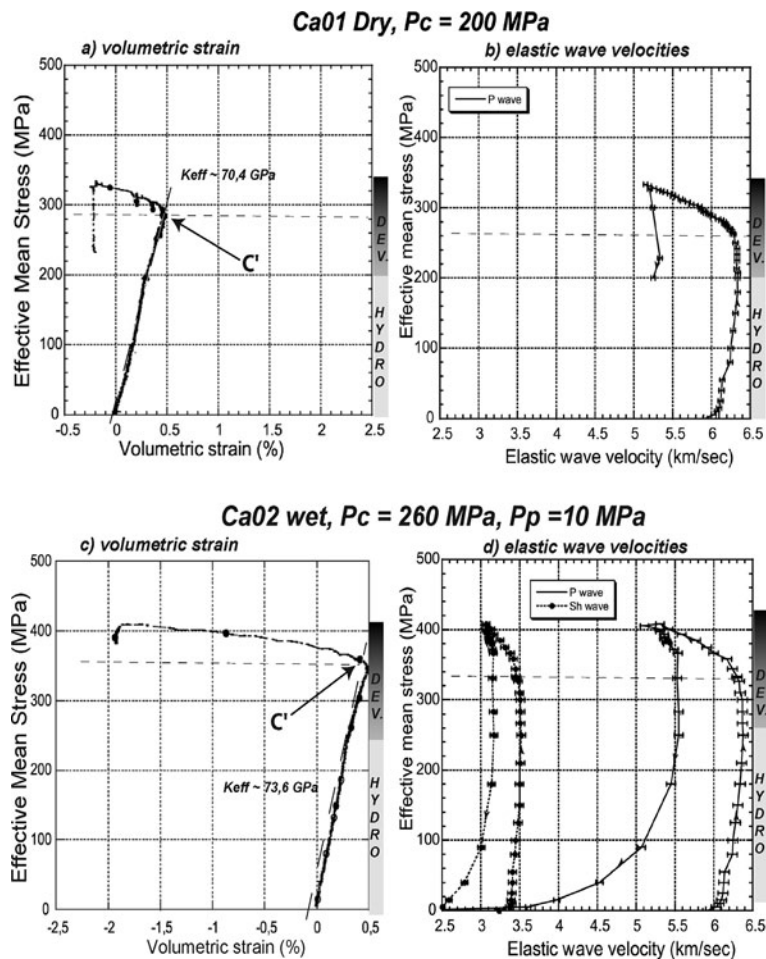Figure 4 shows the coupled evolution of volumetric strain and elastic wave velocities as a

Fig. 4. Coupled evolution of volumetric strain and elastic wave velocities as a function of effective mean stress $[(\sigma_1 + 2\sigma_3)/3 - P_p]$ for experiments performed on Carrara marble. The elastic wave velocities and volumetric strain of the experiment Ca#01 (dry, $P_c = 200$ MPa) are reported in (**a**) and (**c**), respectively, and those of experiment Ca#02 (wet, $P_c = 260$ MPa, $P_p = 10$ MPa) are reported in (**b**) and (**d**) respectively. On the right-hand side of the diagram are reported the conditions at which the measurements were taken. Hydro, hydrostatic; dev, under differential stress. C' indicates the onset of cataclastic dilatancy.

function of effective mean stress for experiments performed on Carrara marble. The effective mean stress is $\mathbf{P} = [(\sigma_1 + 2\sigma_3)/3 - P_\mathrm{p}]$, where σ_1 stands for the axial stress, σ_3 is the confining pressure and P_p the pore pressure; $\mathbf{P}$ is the first stress invariant and allows the representation of the hydrostatic and the differential stresses together on the same plot. The bar on the right-hand side of Figure 4 represents which part of the plot corresponds to hydrostatic stress and which to differential.

Figure 4a & b illustrate, respectively, the volumetric strain and V_p measured during the experiment Ca#01 (dry, $P_\mathrm{c} = 200$ MPa). Up to 275 MPa effective mean stress, the rock mechanical response was elastic and the volumetric strain increased linearly. Static effective compressibility of Carrara marble in the dry regime was equal to 70.4 GPa (Fig. 4a). When onset of cataclastic dilatancy C' was reached (at 275 MPa), the rock started to dilate. Inelastic dilation was also accompanied by non-negligible strain hardening. Figure 4b shows that during the linear elastic phase, P wave velocity exhibits a slight increase due to crack closure. At 200 MPa, P wave reached a plateau value equal to 6.3 km s^{-1} which corresponds to the Voigt–Reuss–Hill average reported for P wave velocity in calcite non-porous aggregates (see for example Birch 1961). Macroscopic dilatancy was associated with a large linear decrease in P wave velocity that actually started a little before C'. One per cent of macroscopic dilation resulted in a decrease of more than 20% in P wave velocities. Therefore, elastic wave velocity measurements appear more sensitive to dilatancy than macroscopic volumetric strain. Very interestingly, V_p increased when the differential stress was removed.

Figure 4c & d show the volumetric strain and V_p and V_s, respectively, v. effective mean stress in experiment Ca#02 (wet, $P_\mathrm{c} = 260$ MPa, $P_\mathrm{p} = 10$ MPa). Comparison of Figure 4a & c shows that the effect of water on the static effective elastic incompressibility of Carrara marble is small. Effective compressibility increased to 73.6 GPa (+5%). This is compatible with an initially small and mainly crack-related porosity of Carrara marble (*c*. 0.5%). The onset of dilatancy C' was reached at 340 MPa effective mean stress. Strain hardening of the sample was less marked than during the dry experiment, whereas macroscopic dilation was much larger. Cataclastic dilatancy was also associated with linear decrease of both P and S wave velocities (Fig. 4d). Total decrease of P wave velocity reached 20% after more than 2% dilation. Comparing this experiment with the previous dry

experiment shows that P wave velocity undergoes a very similar reduction, although the sample dilated more and the strain-hardening coefficient was smaller. This could simply be due to a saturation effect.

The sample was left for relaxation for more than 3 days. During those three days, differential stress slowly decreased, and both P and S wave velocities showed significant increases. After removing the confining pressure, the elastic wave velocities decreased drastically as newly formed cracks re-opened. P wave velocity reached a final value of only 3.3 km s^{-1} at 5 MPa effective confining pressure. Once taken out of the pressure vessel, the sample showed less than 10% seismic anisotropy and no macroscopic localization band.

Figure 5 shows the coupled evolution of volumetric strain and elastic wave velocities as a function of effective mean stress for experiments performed on Solnhofen limestone. In Figure 5a & b, respectively, volumetric strain and P wave velocities are represented for experiment So#02 (dry, $P_\mathrm{c} = 200$ MPa). The rock mechanical response was first elastic and the static effective compressibility of dry Solnhofen limestone was equal to 50.3 GPa (Fig. 5a), which is comparable to what has been previously observed by Baud *et al.* (2000). At 290 MPa effective mean stress, the onset of compaction C^* was reached and the rock started to compact inelastically. The onset of cataclastic dilatancy $C^{*\prime}$ was attained at 335 MPa. Whether the sample was compacting or dilating, cataclastic deformation was associated with significant strain hardening. Figure 5b shows that in the elastic regime, P wave velocity increased linearly and reached a maximum value of 5.75 km s^{-1}. Compaction was not accompanied by an increase in velocity, but conversely, by a decrease. P wave velocity increased instantaneously when the differential stress was unloaded, whereas unloading of the hydrostatic stress was accompanied by a large decrease in P wave velocity due to crack opening. When retrieved, the sample showed no strong elastic wave anisotropy (less than 5%) as well as no macroscopic localization band.

Figures 5c & d show, respectively, the evolution of volumetric strain and of P and S velocities as a function of effective mean stress in experiment So#03 (wet, $P_\mathrm{c} = 260$ MPa, $P_\mathrm{p} = 10$ MPa). Comparing Figure 5a & c, it is possible to observe that the presence of water increased significantly the static effective elastic compressibility of Solnhofen limestone (62.5 GPa, +12%). Water had a smaller increasing effect on P wave velocities, as can be seen when comparing Figure 5b & d, which is
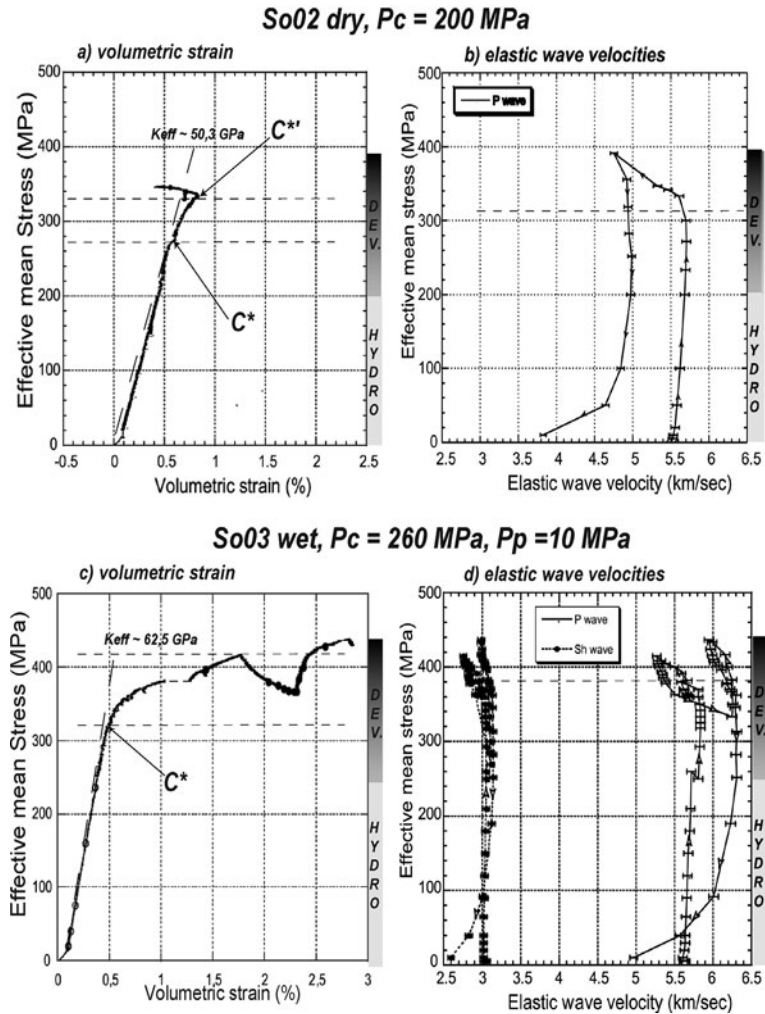
So02 dry, Pc = 200 MPa

Fig. 5. Coupled evolution of volumetric strain and elastic wave velocities as a function of effective mean stress $[(\sigma_1 + 2\sigma_3)/3 - P_p]$ for experiments performed on Solnhofen limestone. The elastic wave velocities and volumetric strain of the experiment So#02 (dry, $P_c = 200$ MPa) are reported in (**a**) and (**c**), respectively, and those of experiment So#03 (wet, $P_c = 260$ MPa, $P_p = 10$ MPa) are reported in (**b**) and (**d**), respectively. On the right-hand side of the diagram are reported the conditions at which the measurements were taken. Hydro, hydrostatic; dev, under differential stress. C^* stands for the onset of cataclastic compaction, while $C^{*\prime}$ indicates the onset of cataclastic dilatancy.

compatible with the fact that, contrary to Carrara marble, the initial porosity in Solnhofen is quite large (c. 4.4%) and mainly equant.

Figure 5c shows that the onset of compaction C^* was reached at 310 MPa effective mean stress. Strain hardening was more important than during the dry experiment. However, no macroscopic cataclastic dilatancy was ever observed. Figure 5d shows that, at first, compaction was not associated with any variation in elastic wave velocities. However, P and S wave

velocities both started to decrease at 360 MPa effective mean stress. The decrease was smaller than during the dry experiment. The sample was then left to relax for 3 days. As differential stress slowly decreased, the sample compacted. P wave velocities increased to finally reach the value of 6.3 km s^{-1}, i.e. the reported Voigt–Reuss–Hill average for P wave velocity in non-porous calcite aggregates. Such behaviour was also observed on S waves. The sample was then reloaded. Velocities started to decrease

again at 370 MPa. Inelastic compaction started when the maximum effective mean stress previously reached during the first cycle was retrieved, i.e. at 410 MPa. The sample was left again for relaxation and after 3 days velocities recovered completely to their maximum value. These results will be discussed more extensively in the next section.

When hydrostatic stress was unloaded, P and S velocities started to decrease as cracks were opening again. Once removed form the pressure vessel, the sample showed no strong elastic wave anisotropy (less than 5%) or macroscopic localization band.

Differential stress relaxation and elastic recovery

During relaxation, the piston position was locked. Differential stress $Q = (\sigma_1 - \sigma_3)$ decreased due to the sample deformation, while pore pressure and confining pressure were kept constant. Samples were left relaxing from 1 h in the case of dry experiments to several days in the case of saturated ones. Because of the machine design, the piston could not be perfectly maintained in position and therefore, some exponentially decreasing small amount of axial strain continued while the relaxation tests were performed (as can be seen in Fig. 7c) – in all the following plots, axial, radial and volumetric strains were measured using strain gauges. As a consequence and to be perfectly right, deformation taking place in the sample was not only composed of true relaxation, but also of a small component of creep. However, in the rest of this paper, we will refer to those tests as relaxation phases anyway. Seismic implications of these results will be discussed in the next section.

Results obtained while Solnhofen limestone and Carrara marble were relaxing in the dry regime (So#02 and Ca#01) are shown in Figure 6. In both experiments, relaxation took place after approximately 5% axial strain. Figure 6a shows the evolution of P wave velocity (plain symbols) and differential stress (empty symbols) v. time. On the figure, the differential stress scale on the right is inverted for easier reading and the timescale is linear. Solnhofen sample So#02 was left for relaxation for 1 h (bottom of Fig. 6a). We can observe that: (1) P wave velocity reached a minimum value when differential stress was maximum; and (2) P wave velocity increased as differential stress was decreasing. Total P wave velocity increase during relaxation was greater than 3%. Differential stress and P wave velocity curves are very
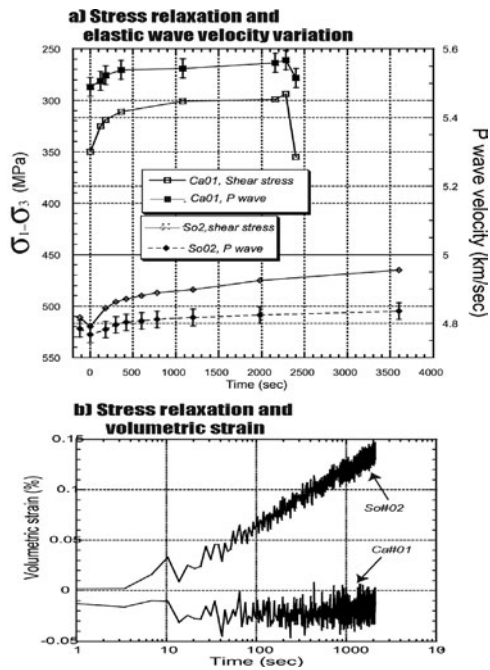
well anti-correlated, so that the stress dependence of P wave velocity is clearly demonstrated.

In the same way, Carrara marble sample Ca#01 was left for relaxation for 45 min (top of Fig. 6a) after approximately 5% axial strain. Again, P wave elastic velocity increased while differential stress decreased, and total P wave velocity increase this time was no larger than 2%. Stress dependence of P wave velocity is clearly observed. More surprising was that when differential stress increased again to the peak value prior to relaxation, P wave velocities immediately resumed to their prior minimum values. It can therefore be concluded that during cataclastic deformation of both Solnhofen limestone and Carrara marble in dry conditions, P wave velocity exhibits an 'elastic like' behaviour, i.e. reversible. Figure 6b shows the evolution of volumetric strain in both samples during the same relaxation tests. Time is in

Fig. 6. Solnhofen limestone and Carrara marble relaxation experiments in the dry regime (So#02 and Ca#01). In both cases, relaxation took place after approximately 10% axial strain. Figure 6a shows the evolution of both P wave velocity (plain symbols) and differential stress (empty symbols) v. time. In (**a**) the differential stress scale on the right-hand side is inverted for easier reading and the timescale is linear. (**b**) Shows the evolution of volumetric strain (measured using strain gauges) in both samples during the same tests. Time is in logarithmic scale.

logarithmic scale. During relaxation, Solnhofen sample So#02 compacted, while Carrara marble sample Ca#01 showed no volumetric change. Hence, elastic wave properties are shown to be much more sensitive to small stress variations than the macroscopic strain.

Results obtained during two different relaxation tests performed on wet Carrara marble sample Ca#02 are shown in Figure 7. The first and second relaxation events took place after approximately 2.5 and 10% axial strain, respectively. Figure 7a shows the evolution of both P wave (empty symbols to be read on the left-hand scale) and S wave (plain symbols to be read on the right-hand scale) v. time. We can see that during both tests P and S wave velocities increased monotonically with time in a logarithmic scale. Increase in velocities was greater during the second relaxation phase, and reached approximately 6% and 3% for P and S wave,

respectively. This was certainly due to larger prior axial strain (c. 10%). Consequently, damage in the rock had been more important before the second test started.

Evolution of differential stress v. time is shown in Figure 7b. During both relaxation phases, differential stress decreased monotonically in the semi-log space. Again, the slope was steeper during the second relaxation, i.e. when the rock had experienced more damage. Figure 7c shows the evolution of axial strain and volumetric strain v. time during both tests. It is important to remember that at such high effective confining stress, Carrara marble porosity is close to zero and mainly crack-related. This explains why, although the sample shortened significantly (approximately 0.4% in 3 days), volumetric strain remained small. The evolution of volumetric strain can be schematically described as follow: a first phase where the rock continued
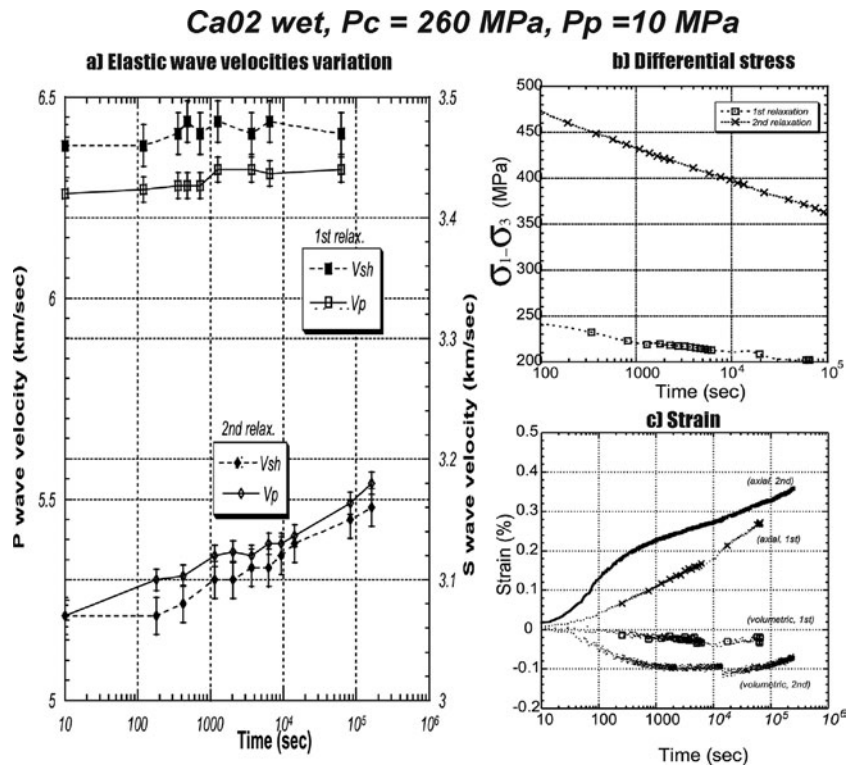

Fig. 7. Carrara marble sample Ca#02 relaxing in the wet regime. First and second relaxation phases took place after approximately 2.5 and 10% axial strain, respectively. (**a**) shows the evolution of both P wave (empty symbols to be read on the left-hand scale) and S wave (plain symbols to be read on the right-hand scale) elastic velocities v. time. Evolution of differential stress is shown in (**b**) while (**c**) shows the evolution of both axial strain and volumetric strain (measured using strain gauges). Time scales are logarithmic.

to dilate, an equilibrium phase where compaction and dilatancy balanced, finally followed by a compaction phase.

Results obtained during two relaxation tests performed on wet Solnhofen limestone sample So#03 after approximately 2.5 and 10% axial strain, respectively, are shown in Figure 8. Figure 8a shows the evolution of P wave (empty symbols to be read on the left-hand scale) and S wave (plain symbols to be read on the right-hand scale) v. time in logarithmic scale. During the first relaxation, increase in velocities was more or less linear with time. Elastic wave velocity increase was also more important during that first test than during the second relaxation, and variation in velocities reached more than 25% (from approximately 5 to 6.3 km s^{-1} in the case of P waves). During the second relaxation, behaviour resembled much of what has been seen previously on Carrara marble: P and S wave velocities increase monotonously and velocity variations reached approximately 6 and 3% for P and S$_h$ waves, respectively. Figure 8c shows that compaction was more important (almost 0.3%) during the first relaxation than during the second relaxation (0.1%). However, decrease in differential stress was comparable (*c.* 150 MPa) and monotonous in both cases, as seen in Figure 8b.

Comparing this figure with Figure 5 indicates that compaction in Solnhofen limestone can be associated both with an increase or decrease in elastic wave velocities. At low strain rates (typically during a relaxation test) compaction is slow and wave velocities are increasing. At fast strain rates (typically during triaxial loadings) compaction is much faster but wave velocities decrease due to increasing damage in the rock. This observation highlights that dilatancy and compaction are transient during cataclastic deformation, probably because their associated mechanisms are in competition. As a consequence, and
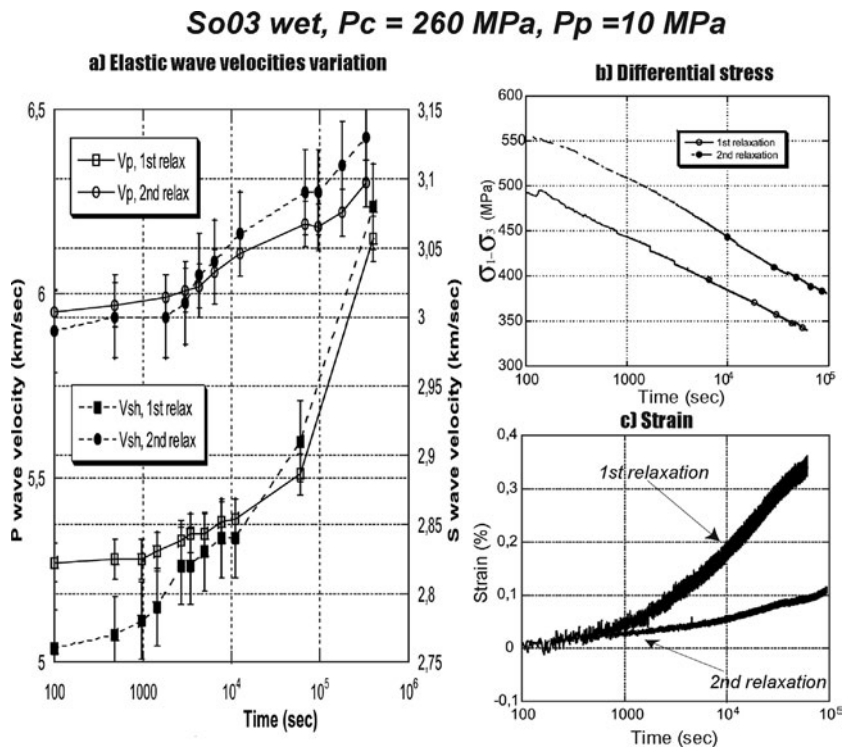

Fig. 8. Solnhofen sample So#03 when relaxing in the wet regime. First and second relaxation phases took place after approximately 2.5 and 10% axial strain, respectively. (**a**) shows the evolution of both P wave (empty symbols to be read on the left-hand scale) and S wave (plain symbols to be read on the right-hand scale) elastic velocities v. time in a logarithmic scale. Evolution of differential stress v. time in logarithmic scale is shown in (**b**), while (**c**) shows the evolution of both axial strain and volumetric strain (measured using strain gauges).

because elastic properties are much more sensitive to cracks than to pores, macroscopic strain and elastic wave velocities are not systematically correlated. Such observation is clear throughout Figures 5–7, and seems to be quite common in porous rocks as it has also been reported recently in high porosity sandstones by Fortin *et al.* (2004). When the fully compacted state is reached, P and S wave velocities should attain a maximum value of approximately 6.3 and 3.2 km s^{-1}, respectively, which are the reported Voigt–Reuss–Hill averages for calcite non-porous aggregates. This stage was apparently reached for sample So#03 and from then, its behaviour resembles that of Carrara marble. This observation is clear when comparing data from the second relaxation tests in Figures 7 and 8.

Microstructural analysis

Figure 9 presents micrographs obtained in the scanning electron microscopy (SEM) of the intact Solnhofen sample (Fig. 9a & b), a sample deformed dry So#02 (Fig. 9c & d) and a sample deformed wet So#03 (Fig. 9e & f). The compressive axis is vertical on all the pictures. The initial porosity of the intact rock appears to be quite heterogeneous, with both equant and elliptical pores. Grain boundaries are serrated and hardly visible, even at high magnification, as in Figure 9b. When deformed in the dry regime (Fig. 9c & d), the initial porosity disappeared and was replaced by a large density of small intergranular cracks located at grain boundaries. In Figure 9d, grain boundaries appear to be opened. Cracks are short (a few tens of micrometres) with large apertures and aspect ratios (between 10^{-1} and 10^{-2}). Furthermore, cracking is well distributed and non-localized, and shows no evidence of anisotropy in its distribution and orientation pattern. Such observation is in agreement with post-deformation elastic wave velocity measurements. In the sample deformed in the wet regime (Fig. 9e & f), initial porosity decreased even more drastically and almost no spherical pores can be seen. Crack density is much lower than in the dry case. Cracks are still located at grain contacts but their aperture appear much smaller (comparing with Fig. 9d). One might also argue that some evidence of dissolution can be seen at several grain contacts. Such features, however, might have been pre-existent in the rock. Figure 10 presents two optical micrographs of Solnhofen samples So#02 and So#03 obtained in cross-polarized light. Irrespective of whether deformation occurred in the dry or wet regime, calcite crystals exhibit extensive twinning that does not pre-exist in the intact rock samples.

Figure 11 presents two optical micrographs of Carrara marble sample Ca#02. The sample was deformed in water-saturated conditions, and on both pictures the axis of compression is vertical. The microstructures of the deformation are quite heterogeneous and takes place both on the intergranular and intragranular scales. As observed in Solnhofen limestone, many cracks are located at grain boundaries and are generally never longer than one or two times the grain size. Voids initiating at the triple junction between grains show evidence of frictional sliding along grain boundary. On the intragranular scale, mechanical twins are present in every single grain at a very high density on both pictures. Bent and kinked twins are also present, as can be seen in Figure 11a, and as was already reported by Fredrich *et al.* (1989). Twin geometries are quite complex, with two and sometimes three sets of active twins in a single grain (see Fig. 11b). In general and depending, of course, on every crystal orientation, twins seem to be oriented more or less vertically. Geometries strongly suggestive of interaction between brittle and plastic deformation mechanisms can be particularly well observed in Figure 11a as the bending of twins often nucleates an intragranular crack. Tullis & Yund (1992) have reported similar observations on feldspar aggregates undergoing cataclastic deformation at a temperature of 300 °C. Again, microstructural observations suggest a complex interplay between plastic deformation and microcracking.

Features observed under the optical microscope and the SEM indicate that deformation mechanisms active during the experiments included: twinning, microcracking and frictional sliding along fractured grain boundaries and, possibly, pressure solution (when saturated). Macroscopic strain and elastic properties evolution depend on the interplay of each of these mechanisms. As previously reported in Carrara marble by Fredrich *et al.* (1989), twinning activity and dislocation glide in calcite grains are likely to be largely responsible for crack nucleation at grain boundaries. Indeed, because of different crystallographic orientations between neighbouring crystals, stress concentrations due to differential strain may facilitate crack nucleation and trigger frictional sliding along fractured grain boundaries. Because of stress concentration effects, granular flow would tend to concentrate around large pores and interplay of several mechanisms (twinning, crack opening and frictional sliding) would therefore be needed to induce macroscopic compaction.
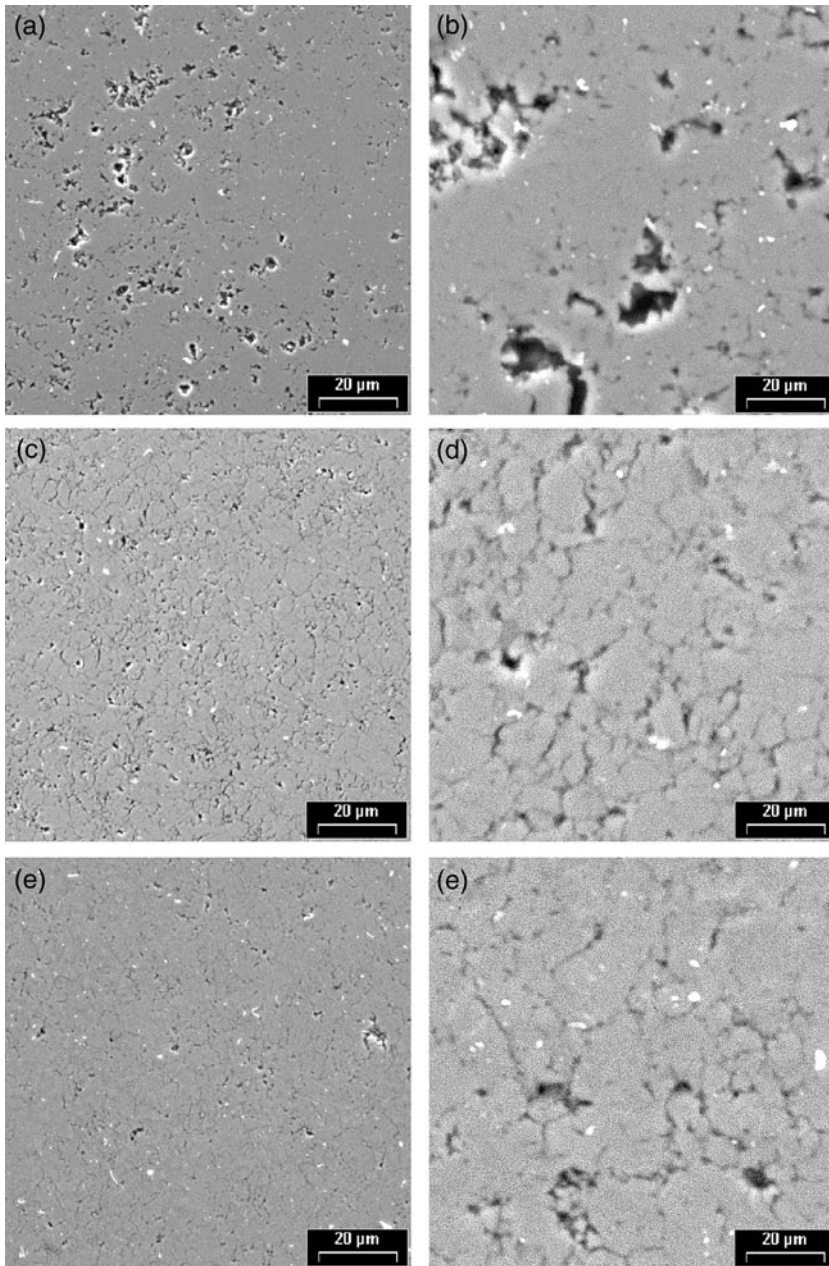
Fig. 9. Series of secondary electron SEM images of (**a**) and (**b**) intact, (**c**) and (**d**) deformed dry (So#02), and (**e**) and (**f**) deformed wet (So#03) Solnhofen samples. The compressive axis is vertical on the pictures. Scale is 20 μm in (a), (c) and (e), and 5 μm in (b), (d) and (f).

Mechanical analysis

In this section we analyse our results in the light of previous studies performed on Solnhofen limestone and Carrara marble.

Damage and dilatancy in carbonate rocks

Onset of crack propagation and frictional sliding. Figure 12 compares the onsets of dilatancy for both Solnhofen limestone and
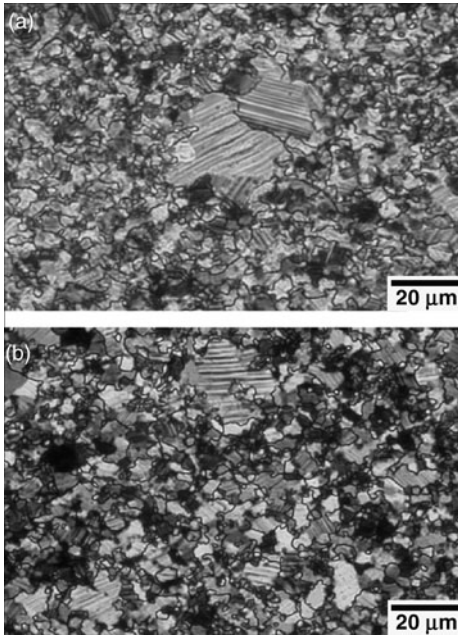
Fig. 10. Optical micrographs obtained in cross-polarized light of Solnhofen samples (**a**) So#02 and (**b**) So#03 deformed in the dry and wet regimes, respectively. Compression direction is vertical in all photographs. Note the twins oriented at a high angle to the compression direction in the largest grains. These twins developed during the experiments, as the undeformed material does not contain this type of twin.
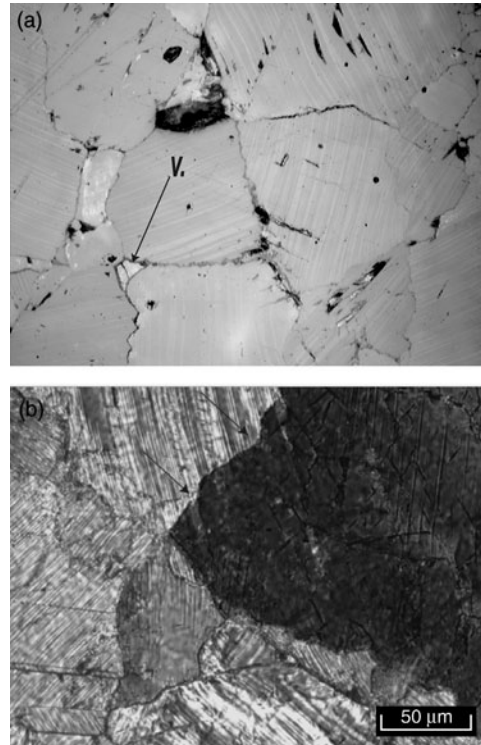

Fig. 11. Optical micrographs in (**a**) reflected light and (**b**) cross-polarized light of deformed Carrara marble sample Ca#02. In both photomicrographs, the axis of compression is vertical. In (a) V points to a void at a grain triple junction. In (b) the arrows point towards evidence of slip in the geometry of a grain boundary (top right-hand corner)

Carrara marble determined in this study with those reported by various authors in the literature (see Table 2). In Figure 12, it appears clear that maximum compressive stress σ_1 at onset of dilatancy evolves linearly with confining pressure. The onset of dilatancy is also much smaller in Carrara marble than in Solnhofen limestone.

Using the well-established wing crack model (Ashby & Sammis 1990; Fredrich *et al.* 1990; Baud *et al.* 2000) has proved to be of particular help in understanding the onset of crack propagation in rocks under compression. In axisymmetric compression, and for a randomly oriented distribution of cracks, the stress conditions for a tensile wing crack to propagate in mode I from a sliding crack tip are (see, for example, Lehner & Kachanov 1996):

$$\sigma_1 = \frac{\sqrt{1+\mu^2}+\mu}{\sqrt{1+\mu^2}-\mu}\sigma_3 + \frac{\sqrt{3}}{\sqrt{1+\mu^2}-\mu}\frac{K_{\text{Ic}}}{\sqrt{\pi l}}$$

(1)

where σ_1 and σ_3 stand for the axial stress and confining pressure, respectively. μ is the internal friction coefficient of the material, K_{Ic} the critical intensity factor (or fracture toughness) for a crack to propagate in mode I and l is the initial length of the pre-existing crack or default. In such a simple model, but widely used in geomechanics, the slope of the dilatancy envelope depends solely on μ. Assuming that μ is constant, the dilatant envelope is a straight line (in the space (σ_1, σ_3)) whose origin depends on the surface energy of the crack and on its length. According to Figure 12, best fit of equation (1) gives a value for the internal friction coefficient equal to 0.54 and 0.56 for Solnhofen limestone and Carrara marble, respectively. Such results are comparable with former values obtained by Ashby & Sammis (1990) ($\mu = 0.55$) and Baud *et al.* (2000) ($\mu = 0.53$) for Solnhofen limestone, and very close to the
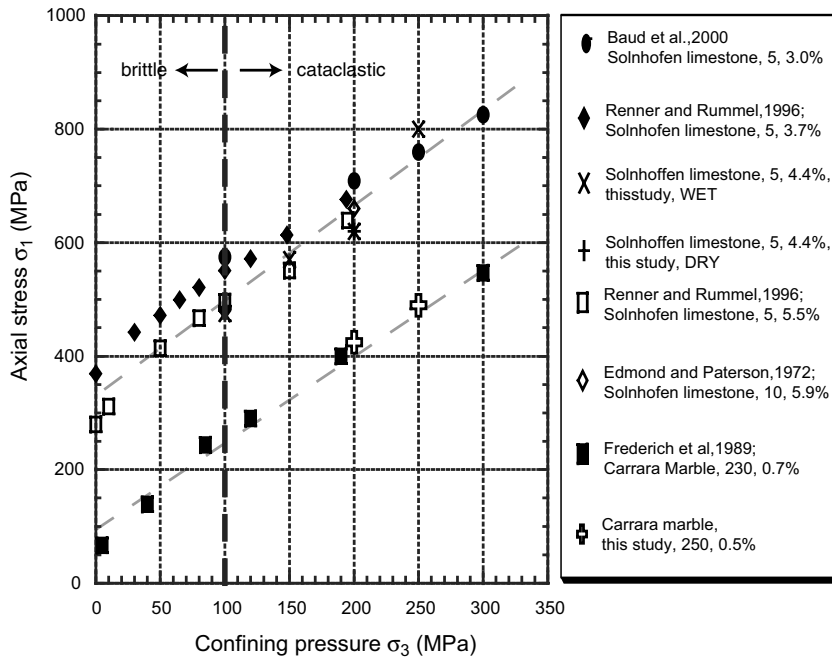
Fig. 12. Comparison in $\sigma_1 - \sigma_3$ space of the onsets of dilatancy for Solnhofen limestone and Carrara marble, as reported in the literature and this study.

value found by Fredrich *et al.* (1990) ($\mu = 0.5$) in Carrara marble. The best fit for $K_{Ic}/\sqrt{\pi l}$ was found to be 124 MPa for Solnhofen limestone and 27 MPa for Carrara marble. Since both rocks are composed of 99% calcite, K_{Ic} should be equal in both rocks. In our case, assuming that $K_{Ic} = 0.2$ MPa m$^{1/2}$, as reported by Atkinson & Avdis (1980), we find an initial crack length of $2l \approx 3$ μm and $2l \approx 70$ μm for Solnhofen limestone and Carrara marble, respectively. The initial crack length ratio is approximately 20 when the grain size ratio between Solnhofen limestone and Carrara marble is about 30. These results are compatible with our microstructural analysis. In the case of Solnhofen limestone, initial porosity also seems

to be a key issue and dilatancy occurs at lower stress with increasing porosity. Such an observation has already been reported by Baud *et al.* (2000) in terms of peak stress and could be explained by the fact that initial damage in the rock is likely to scale with initial porosity.

Cataclastic deformation and crack nucleation. Calcite is well known to require relatively low shear stresses to initiate twinning and slip, even at room temperature: Turner *et al.* (1954) and Griggs *et al.* (1960) obtained values of the order of 145–216 MPa for *f*-slip and *r*-slip dislocation glide, respectively. In addition, *e*-twinning in calcite crystal has been reported to be triggered for even smaller stresses.

Table 2. *Compilation of stress values at which the onset of dilatancy C′ and threshold of macroscopic dilatancy C*′ were observed in Carrara marble and Solnhofen limestone, respectively, during our experiments*

	Confining pressure P_c (MPa)	Pore pressure P_p (MPa)	Effective mean stress **P** (MPa)	Differential stress **Q** (MPa)
C′	Carrara		marble	
Ca#01	200	dry	275	225
Ca#02	260	10	340	270
C′	Solnhofen		limestone	
So#2	200	dry	335	405

As shown by our microstructural analysis, during cataclastic deformation, cracks seem to nucleate preferably at grain contacts and boundaries. Baud *et al.* (2000) suggested that microcracking could be due to dislocation pile-ups. In such a model, if the dislocations pile-up at an obstacle (for example at a grain boundary), tensile stress concentrations nucleate a crack (Stroh 1957; Wong 1990).

On the other hand, microstructural observations reported by Fredrich *et al.* (1990) and ourselves in this paper showed that interplay between twinning and crack nucleation are intense during deformation. At least one source of cracking might be twin intersections, as seen in Figure 11, that could depend inversely on grain size, as is suggested when comparing twin density between Figures 10 and 11.

However, two paradoxes can be pointed out. First, we observed throughout our experiments the decoupling of macroscopic strain and elastic properties. For example, during our experiment Ca#02 (Fig. 4c & d), dilatancy was observed to be very large (2%) with small effects on elastic properties. Second, and as noted originally by Baud *et al.* (2000), the data suggest a slight dependence of $C^{*\prime}$ on pressure, whereas dislocation pile-up models or twin–crack interaction models predict it to be pressure independent (for initiation shear stress). Figure 12 seems to suggest that if cracks can be nucleated by dislocation pile-up or by twinning, damage and dilatancy is nevertheless due to frictional sliding on these newly formed crack surfaces.

Compaction mechanics and recovery in Solnhofen limestone

Effect of initial porosity and water. In their study of compaction and failure modes in Solnhofen limestone, Baud *et al.* (2000) performed experiments in the dry regime only, on samples with an average porosity of 3% and an average grain size of 5 μm. As previously mentioned, our experiments were performed on a block whose initial porosity was 4.4%, both in dry and wet conditions. Four additional experiments were performed on samples coming from the same block (Schubnel 2003), in the wet regime, at the State University of New York in Stony Brook. Table 3 compiles the values of effective mean stress **P** and differential stress **Q** at which the onset of compaction C^* (as defined by Wong *et al.* 1997) were observed in that block.

A comparison with data previously obtained by Baud *et al.* (2000) is plotted in Figure 13. It shows that water enhances compaction greatly. At a given confining pressure, decrease in differential stress at the onset of compaction can be as large as 150 MPa. This has already been shown by Rutter (1986) and could be explained in three different ways: (1) the presence of water increases single crystal plasticity; (2) pressure solution takes place and accounts for the early observed compaction; and (3) water has a lubricating effect.

Variation in porosity also seems to have a small reduction effect on the onset of compaction: C^* for experiment So#03 falls a little lower than the compactive envelope previously obtained by Baud *et al.* (2000). The latter observation is confirmed by a recent general study performed on the compaction of several carbonate rocks (Vajdova *et al.* 2003).

Baud *et al.* (2000) and Vajdova *et al.* (2004) modelled the behaviour of limestones using Curran & Carroll's (1979) model of porous void compaction. In this model, compaction occurs when a pressure-independent plastic yield criterion, σ_Y (or von Mises criterion), is reached. Carroll (1980) predicted that initial yield in hydrostatic compression occurs at the macroscopic pressure:

$$P^* = \frac{2}{3}\sigma_Y \left[1 - \frac{2\mu\phi}{2\mu + \sigma_Y(1 - \phi)} \right] \quad (2)$$

Table 3. *Compilation of stress values at which the onset of compaction C^* was observed in Solnhofen limestone. In our block of Solnhofen limestone, initial porosity was 4.4%. The superscripts * indicates experiments that have been performed in the Rock Mechanics Laboratory of SUNY at Stony Brook*

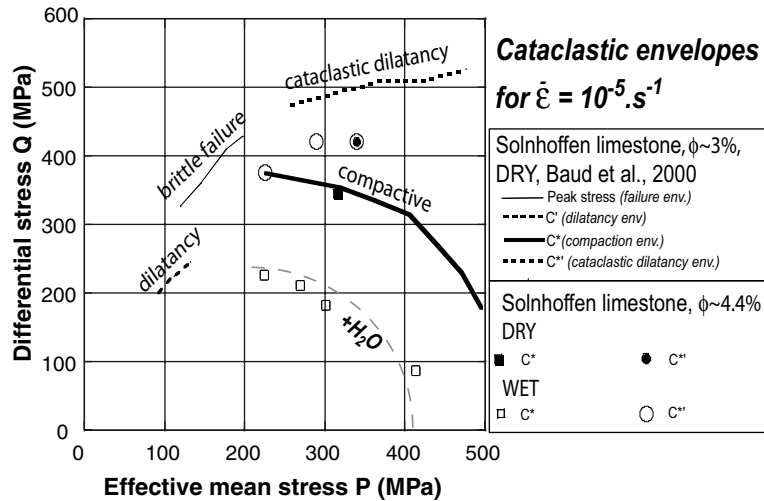| Solnhofen limestone	Confining pressure P_c (MPa)	Pore pressure P_p (MPa)	Effective mean stress **P** (MPa)	Differential stress **Q** (MPa)
C^*				
So#12*	160	10	225	225
So#2	200	dry	290	270
So#07*	210	10	270	210
So#3	260	10	310	180
So#11*	390	10	410	90

Fig. 13. Comparison of our results to those previously obtained by Baud *et al.* (2000). **P** is the effective mean stress and **Q** the differential stress.

where μ is the shear modulus and ϕ the initial porosity. Baud *et al.* (2000) concluded that, in order for Curran & Carroll's (1979) model to provide a reasonable fit of Solnhofen limestone's compactive envelope, σ_Y needed to be larger (*c.* 975 MPa) than experimentally determined values for single-crystal plasticity in calcite. When water is present, we found the value of σ_Y to decrease to approximately 600 MPa, which, in any case, is still much larger than experimentally determined values for single-crystal plasticity in calcite. It is interesting to add that investigating the compaction of dry Tavel limestone (9% porosity, 5 μm average grain size), Vajdova *et al.* (2004) showed that Curran & Carroll's (1979) model overestimated the yield criterion in the same way. In light of this paradox, one can suggest that because the von Mises criterion requires five independent slip systems (Paterson 1969) for homogeneous plastic flow to occur in the proximity of a pore surface, the plastic yield criterion σ_Y was likely to be larger than the one observed for single slip systems. However, and as shown on Figure 10, twinning of calcite was observed. Paterson (1969, 1978) showed that when e-twinning in calcite is activated, the combination of twinning and only one slip mode is equivalent to five independent slip systems. The problem remains therefore unanswered but two hypothesis can be drawn: (1) plastic deformation mechanisms like twinning and dislocation glide are grain size sensitive; and (2) operative mechanisms also involve

pressure-dependant frictional processes. The observation of evidence for frictional sliding along grain boundaries in our microstructural analysis and the observed effect of water on compactive yield stresses may point towards the latter solution.

Recovery of elastic properties. Cyclic loading in the brittle regime is characterized generally by a large hysteresis between loading and unloading. However, there is an almost elastic region when changing the state of stress, with very little hysteresis and almost constant P and S wave velocities. Our experimental observations of P and S wave evolutions in low-porosity calcite rocks deforming in the cataclastic regime showed that such a 'deadband', typical of hysteresis cycles where the velocities remained constant during loading and unloading, does not exist. On the contrary, the apparent elastic properties of the rock showed a high stress dependency and varied immediately when the stress state was changed.

The simplest option to explain apparent recovery of elastic properties is to assume that it is partly due to back-sliding on cracks. If so, the onset of back-sliding on a crack is simply given by:

$$\Delta\tau = \mu\Delta\sigma_n \qquad (3)$$

where $\Delta\tau$ and $\Delta\sigma_n$ correspond to the variations in shear and normal stresses on the crack surface after the loading changed direction. In the case of an axisymmetric unloading, Kachanov

(1982a, b) showed that the macroscopic envelope of the 'dead band' for a family of randomly oriented cracks is a hyperbola in the (σ_1, σ_3) space. At effective confining pressures higher than 200 MPa, and assuming a friction coefficient of approximately 0.5 for calcite, frictional back-sliding on crack surfaces cannot be initiated before axisymmetric extension state is reached and, therefore, back-sliding cannot account for any observations of recovery.

However, if we assume that the friction coefficient is a state variable (as in the framework of Rate and State Friction; see, for example, Marone 1998), recovery can be due to contact strengthening. Under contact loading, particle surface may deform inelastically (for example due to dissolution of crack asperities or visco-elastic interpenetration of crack surfaces) and cohesion between contacting surfaces may increase. In such a way, strengthening derives from growth of contact area (Dietrich & Kilgore 1994) via chemically assisted mechanisms (Frye & Marone 2002). In the laboratory, contact healing has been widely observed and was shown to depend on the logarithm of contact duration (e.g. Beeler & Tullis 1997), which has also been observed in our experiments. However, in our relaxation experiments, inferring internal friction coefficient cannot be straightforward and further analysis would be needed to quantify the exact variations of friction coefficient with time.

Conclusions and implications for fault zones

In the cataclastic regime, our experimental results shows that during the deformation of low-porosity calcite-rich rocks, dilatant (crack opening and sliding, void creation) and compactive (pressure solution, pore closure) micromechanisms are not exclusive and may interact. In the case of an initially porous rock like Solnhofen limestone, the evolution of apparent elastic properties (mainly sensitive to crack density) and macroscopic volumetric strain (more sensitive to equant porosity) is not systematically correlated and depends on the strain rate, the solid stress conditions and the pore pressure. Our data suggest that twinning activity and dislocation pile-up in calcite polycrystals participate in the nucleation of cracks at grain boundaries. Macroscopic compaction occurs when frictional sliding is triggered on those boundary cracks.

During our experiments, damage and recovery of P–S elastic wave velocities were observed to be transient phenomena that are associated with distinct elastic wave velocity variations. In our experiments, these variations could be large and fast, especially in the presence of fluid ($>10\%$ in a couple of days, at room temperature). Crack nucleation and propagation was shown to be responsible for increasing damage, while recovery of elastic properties is thought to be due to re-strengthening of grain contacts.
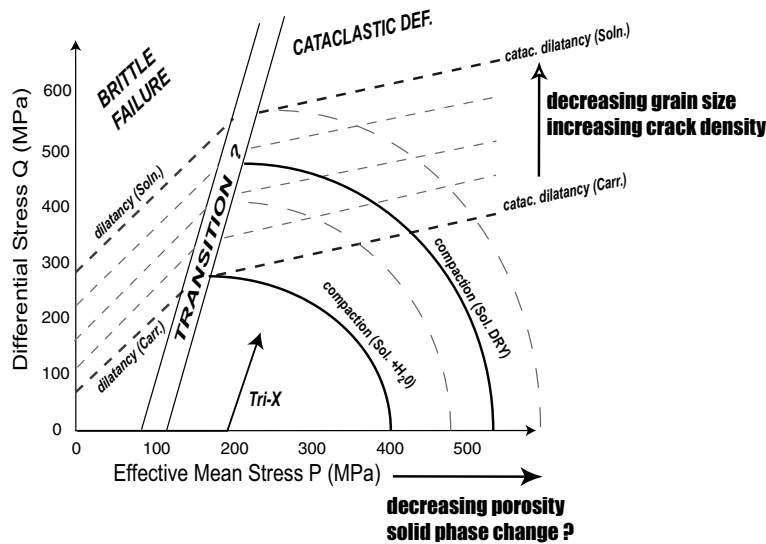

Fig. 14. Schematical deformation map in the principal stress space for calcite rocks according to our experimental observations. In the principal stress space, we recall that the triaxial loading path has a slope equal to 3.

Recent *in situ* velocity monitoring field studies (Crampin *et al.* 2002) where temporal changes of both P and S velocities were observed before earthquakes and volcanic eruptions could be explained by similar mechanisms.

As fault gouges are highly complex materials, experimentalists need to find good analogues for simple and relevant laboratory experiments. Figure 14 summarizes schematically the deformation map in the principal stress space for calcic rocks according to our experimental observations. In this space, we recall that the triaxial loading path has a slope equal to 3. In the cataclastic domain, we see that the dilatant and compactive envelopes are overlapping. The observed macroscopic strain was shown to be a function of both strain rate and pore pressure, and the dominant mechanism is selected depending on its kinetics. On one hand, increasing mean stress seems to favour porosity decrease (and possible solid-phase changes like the calcite–aragonite phase transition). On the other hand, increasing differential stress is generally accompanied by grain size reduction and an increase in the crack density.

One of the main parameters controlling the earthquake cycle is known to be not only the differential stress but also the pore pressure (Rice 1992). Owing to the new fracture network and increase in fault gouge permeability, poro-elasticity predicts a viscous release of the pore pressure during the co- and post-seismic phases. Such variations in pore pressure suggest that the stress path a gouge material experiences during the seismic cycle is likely to be much more horizontal than regular triaxial paths in the **PQ** plot. This last observation highlights the limitations of the 'regular triaxial' stress path when trying to understand fault gouge behaviour or the brittle–ductile transition. Recent analysis of the seismic cycle by Miller (2002) and Shapiro *et al.* (2003) are pointing towards that way. As a consequence, we believe it is necessary to perform experiments along different stress paths (for example fluid pressurization) in order to elucidate the natural failure processes and their interplay. Further experimental investigations of the cataclastic regime using acoustic emission localization techniques, could, potentially, provide insights.

References

ASHBY, M.F. & SAMMIS, C.G. 1990. The damage mechanics of brittle solids in compression. *Pure and Applied Geophysics*, **133**, 489–521.

ATKINSON, B.K. & AVDIS, V. 1980. Fracture mechanics parameters of some rock-deforming minerals determined using an indentation technique. *International Journal of Rock Mechanics and Mining Science, Geomechanical Abstract*, **17**, 383–386.

BAUD, P., SCHUBNEL, A. & WONG, T.-F. 2000. Dilatancy, compaction and failure mode in Solnhofen limestone. *Journal of Geophysical Research*, **105**, 19 289–19 320.

BEELER, N.M. & TULLIS, T.E. 1997. The roles of time and displacement in velocity-dependent volumetric strain of fault zones. *Journal of Geophyscial Research*, **102**, 22 595–22 609.

BIRCH, F. 1961. The velocity of compressional waves in rocks up to 10 kbars, part 2. *Journal of Geophysical Research*, **66**, 2199–2224.

BYERLEE, J.D. 1968. Brittle–ductile transition in rocks. *Journal of Geophysical Research*, **73**, 4741–4750.

CRAMPIN, S., VOLTI, T., CHASTIN, S., GUDMUNDSSON, A. & STEFANSSON, R. 2002. Indication of high pore-fluid pressure in a seismically-active fault zone. *Geophysical Journal International*, **151**, F1–F5.

CURRAN, J.H. & CARROLL, M.M. 1979. Shear stress enhancement of void compaction. *Journal of Geophysical Research*, **84**, 1105–1112.

DIETERICH, J.H. & KILGORE, B.D. 1994. Direct observation of frictional contacts – new insights for state dependent properties. *Pure and Applied Geophysics*, **143**, 283–302.

EDMOND, J.M. & PATERSON, M.S. 1972. Volume changes during the deformation of rocks at high pressure. *International Journal of Rock Mechanics and Mining Science*, **9**, 161–182.

FORTIN, J., SCHUBNEL, A. & GUÉGUEN, Y. 2005. Elastic wave velocities and permeability evolution during compaction of Bleuswiller sandstone. *International Journal of Rock Mechanics and Mining Science*, in press.

FREDRICH, J.T., EVANS, B. & WONG, T.-F. 1989. Micromechanics of the brittle to plastic transition in Carrara marble. *Journal of Geophysical Research*, **94**, 4129–4145.

FREDRICH, J.T., EVANS, B. & WONG, T.-F. 1990. Effect of grain size on brittle and semi-brittle strength: implications   for   micromechanical

modelling of failure in compression. *Journal of Geophysical Research*, **95**, 10 907–10 920.

FISHER, G.J. & PATERSON, M.S. 1992. Measurement of permeability and storage capacity in rocks during deformation at high temperature and pressure. *In*: EVANS, B. & WONG, T.-F. (eds) *Fault Mechanics and Transport Properties of Rocks.* Academic Press, San Diego, CA, 213–252.

FRYE, K.M. & MARONE, C. 2002. Effect of humidity on granular friction at room temperature. *Journal of Geophysical Research*, **107**, art. no. 2309.

GRIGGS, D.T., TURNER, F.J. & HEARD, H.C. 1960. Deformation of rocks at 500° to 800°. *In*: GRIGGS, D.T. & HANDIN, J. (eds) *Rock Deformation*. Geological Society of America Memoir, **79**, 39–104.

HEARD, H.C. 1960. Transition from brittle fracture to ductile flow in Solnhofen limestone as a function of temperature, confining pressure and interstitial fluid pressure. *In*: GRIGGS, D.T. & HANDIN, J. (eds) *Rock Deformation*. Geological Society of America Memoir, **79**, 193–226.

KACHANOV, M. 1982*a*. A microcrack model of rock inelasticity, part I: Frictional sliding on microcracks. *Mechanics of Materials*, **1**, 19–27.

KACHANOV, M. 1982*b*. A microcrack model of rock inelasticity, part II: Propagation of microcracks. *Mechanics of Materials*, **1**, 29–41.

LEHNER, F. & KACHANOV, M. 1996. On modelling 'wing-cracks' forming under compression. *International Journal of Fracture*, **77**, R69.

MARONE, C. 1998. Laboratory-derived friction laws and their application to seismic faulting. *Annual Review of Earth and Planetory Science*, **26**, 643–696.

MILLER, S.A. 2002. Properties of large ruptures and the dynamical influence of fluids on earthquakes and faulting. *Journal of Geophysical Research*, **107**, 2182.

PATERSON, M.S. 1958. Experimental deformation and faulting in Wombeyan marble. *Geological Society Bulletin*, **69**, 465–476.

PATERSON, M.S. 1969. The ductility of rocks. *In*: ARGON, A.S. (ed.) *Physics and Crystal Strength*. MIT Press, Cambridge, MA.

PATERSON, M.S. 1978. *Experimental Rock Deformation: The Brittle Field*. Springer, New York.

RENNER, J. & RUMMEL, F. 1996. The effect of experimental and microstructural parameters on the transition from brittle failure to cataclastic flow of carbonate rocks. *Tectonophysics*, **258**, 151–169.

RICE, J.R. 1992. Fault stress states, pore pressure distributions and the weakness of the San Andreas fault. *In*: EVANS, B. & WONG, T.-F. (eds) *Fault Mechanics and Transport Properties of Rocks*. Academic Press, London, 475–503.

ROBERTSON, E.C. 1955. Experimental study of the strength of rocks. *Geological Society of America Bulletin*, **66**, 1275–1314.

RUTTER, E.H. 1972. The effects of strain-rate chages on the strength and ductility of Solnhofen limestone at low temperatures and confining pressures. *International Journal of Rock Mechanics and Mining Science*, **9**, 183–189.

RUTTER, E.H. 1974. The influence of temperature, strain rate and interstitial water in the deformation of calcite rocks. *Tectonophysics*, **22**, 331–334.

RUTTER, E.H. 1986. On the nomenclature of failure transitions in rocks. *Tectonophysics*, **122**, 381–387.

SCHUBNEL, A. 2003. *Mécanismes de la dilatance et de la compaction dans les roches de la croûte*. Thèse de doctorat de l'Institut de Physique du Globe de Paris.

SHAPIRO, S.A., PATZIG, R., ROTHERT, E. & RINDSCHWENTNER, J. 2003. Triggering of seismicity by pore-pressure perturbations: Permeability-related signatures of the phenomenon. *Pure and Applied Geophysics*, **160**, 1051–1066.

STROH, A.N. 1957. A theory of the fracture of metals. *Advances in Physics*, **6**, 418–465.

TULLIS, J. & YUND, R.A. 1992. The brittle–ductile transition in feldspar aggregates: and experimental study. *In*: EVANS, B. & WONG, T.-F. *Fault Mechanics and Transport Properties of Rocks*. Academic Press, San Diego, CA, 89–117.

TURNER, F.J., GRIGGS, D.T. & HEARD, H.C. 1954. Experimental deformation of calcite crystals. *Geological Society America Bulletin*, **65**, 883–934.

VAJDOVA, V., BAUD, P. & WONG, T.-F. 2004. Compaction, dilatancy and failure in porous carbonate rocks. *Journal of Geophysical Research*, **109**, art. B05204.

WONG, T.-F. 1990. Mechanical compaction and the brittle-ductile transition in porous sandstones. *In*: KNIPE, R.J. & RUTTER, R.H. (eds) *Deformation Mechanisms, Rheology and Tectonics*. Geological Society, London, Special Publications, **54**, 111–112.

WONG, T.-F., DAVID, C. & ZHU, W. 1997. The transition from brittle faulting to cataclastic flow in porous sandstones: Mechanical deformation. *Journal of Geophysical Research*, **102**, 3009–3025.